Characterising energy transfer upconversion in Nd-doped vanadates at elevated temperatures

S. CANTE,* S. J. BEECHER, AND J. I. MACKENZIE

Optoelectronics Research Centre, University of Southampton, Southampton SO17 1BJ, UK
*s.cante@soton.ac.uk

Abstract: The Energy Transfer Upconversion (ETU) macroparameter is measured for Nd-doped $GdVO_4$ and YVO_4 samples at temperatures ranging from Room Temperature (RT) to $450K$, by means of a simple and automated z-scan technique. Furthermore, the ground state absorption cross section into the $^2H_{9/2} +^4 F_{5/2}$ energy levels is characterised for both crystals over the same range of temperatures. The 808 nm π-polarisation absorption cross section is found to decrease from (58.6 ± 0.2) pm^2 to (30.9 ± 0.6) pm^2 for Nd:YVO_4 and (54.0 ± 0.3) pm^2 to (25.7 ± 0.5) pm^2 for Nd:$GdVO_4$, from RT to $450K$. Over the same range the ETU coefficient decreases from $(3.2 \pm 0.7)\ 10^{-16}\ cm^3/s$ to $(1.8 \pm 0.4)\ 10^{-16}\ cm^3/s$ and $(5.0 \pm 0.5)\ 10^{-16}\ cm^3/s$ to $(3.4 \pm 0.2)\ 10^{-16}\ cm^3/s$ for 0.6at.% and 1at.% Nd:YVO_4 respectively, and $(3.3 \pm 0.5)\ 10^{-16}\ cm^3/s$ to $(0.8 \pm 0.2)\ 10^{-16}\ cm^3/s$ and $(5.5 \pm 0.5)\ 10^{-16}\ cm^3/s$ to $(3.1 \pm 0.3)\ 10^{-16}\ cm^3/s$ for 0.5at.% and 1.1at.% Nd:$GdVO_4$.

OCIS codes: (190.7220) Upconversion, (140.3530) Lasers, neodymium, (300.1030) Absorption.

References and links

1. T. Y. Fan and R. L. Byer, "Modeling and CW Operation of a Quasi-Three-Level 946 nm Nd:YAG Laser," IEEE J. Quantum Electron. **23**(5), 605–612 (1987).
2. W. P. Risk, "Modeling of longitudinally pumped solid-state lasers exhibiting reabsorption losses," J. Opt. Soc. Am. B **5**(7), 1412–1423(1988).
3. S. Bjurshagen and R. Koch, "Modeling of Energy-Transfer Upconversion and Thermal Effects in End-Pumped Quasi-Three-Level Lasers," Appl. Opt. **43**(24), 4753–4767 (2004).
4. V. Ostroumov, T. Jensen, J.-P. Meyn, G. Huber, and M. A. Noginov, "Study of luminescence concentration quenching and energy transfer upconversion in Nd-doped $LaSc_3(BO_3)_4$ and $GdVO_4$ laser crystals," J. Opt. Soc. Am. B **15**(3), 1025–1060 (1998).
5. Y.F. Chen, C.C. Liao, Y.P. Lan, and S.C. Wang, "Determination of the Auger upconversion rate in fiber-coupled diode end-pumped Nd:YAG and Nd:YVO_4 crystals," Appl. Phys. B **70**(4), 487–490 (2000).
6. R. Yan, S. J. Yoon, S. J. Beecher, and J. I. Mackenzie, "Measuring the elevated temperature dependence of upconversion in Nd:YAG," IEEE J. Sel. Top. Quantum Electron. **21**(1), 1–7 (2015).
7. Y. Sato and T. Taira, "Temperature dependencies of stimulated emission cross section for Nd-doped solid-state laser materials," Opt. Mater. Express **2**(8), 1076–1087 (2012).
8. J. O. White and C. E. Mungan, "Measurement of up-conversion in Er:YAG via z-scan," J. Opt. Soc. Am. B **28**(10), 2358–2361 (2011).
9. S. J. Yoon, R. P. Yan, S. J. Beecher, and J. I. Mackenzie, "Concentration dependence of energy transfer upconversion in Nd:YAG," Opt. Mater. Express **5**(5), 926–931 (2015).
10. W. J. Lima, V. M. Martins, A. F. G. Monte, D. N. Messias, N. O. Dantas, M. J. V. Bell, and T. Catunda, "Energy transfer upconversion on neodymium doped phosphate glasses investigated by Z-scan technique," Opt. Mater. Express **35**(9), 1724–1727 (2013).
11. S. Goldring, R. Lavi, V. Lupei, "Decay dynamics of excited Nd^{3+} ions in YVO_4 following weak excitation," IEEE J. Quantum Electron. **46**(2), 169–181 (2010).
12. S. Guy, C. L. Bonner, D. P. Shepherd, D. C. Hanna, A. C. Tropper, and B. Ferrand, "High-inversion densities in Nd:YAG: up-conversion and bleaching," IEEE J. Quantum Electron. **34**(5), 900–909 (1998).
13. C. Czeranowsky, "Resonatorinterne Frequenzverdopplung von diodengepumpten Neodym-Lasern mit hohen Ausgangsleistungen im blauen Spektralbereich," Dissertation, Universitat Hamburg (2002).
14. J. W. Kim, J. I. Mackenzie, and W. a. Clarkson, "Influence of energy-transfer-upconversion on threshold pump power in quasi-three-level solid-state lasers," Opt. Express **17**(14), 11935–11943 (2009).
15. D. C. Brown, R. Nelson, and L. Billings, "End-cooled Nd:YVO_4 Diode-pumped Laser," Appl. Opt. **36**(33), 2–4 (1991).

1. Introduction

Nd-doped vanadate crystals are widely used in diode-pumped solid-state lasers. Compared to Nd:YAG, both Nd:YVO$_4$ and Nd:GdVO$_4$ have a higher absorption cross section at 808 *nm* (π-pol), coupled with a larger emission cross section, making it possible to achieve much higher gains per unit length. Most of their key spectroscopic properties have been largely investigated and characterised in order to model and optimise laser performance. However, some parameters have not yet been determined with sufficient precision or reported at all, with consequent difficulties in making a reliable choice of design parameters, e.g. the Energy Transfer Upconversion (ETU) parameter and the temperature dependence of the absorption cross section.

Vanadate crystals are typically employed in lasers operating on the strongest 1.06 μm emission line; however, the lower gain quasi-four-level system operating on the 0.9 μm transition could potentially be quite efficient, thanks to a lower quantum defect between pump and output wavelengths. As the latter transition suffers reabsorption losses and it has lower emission cross section, it is susceptible to the detrimental thermal effects associated with the waste heat deposited during the excitation processes [1–3]. As such, its laser performance could be improved if key contributors to these effects are well characterised.

Parasitic effects like ETU are also deleterious for transitions that require high-irradiance pumping, such as the 0.9 μm quasi-four-level ($^4F_{3/2} \rightarrow ^4 I_{9.2}$) Nd^{3+} system, as they compromise the already relatively-low gain [3]. The ETU process (Fig. 1), in most Nd-doped hosts, leads to the excited ion relaxing back to the $^4F_{3/2}$ level, thus reducing the upper laser level population by one. Waste heat is produced via the non-radiative decay channels of the excited ions, adding to the other sources of heat. Depending on its strength, ETU can potentially be catastrophic for laser operation on the 0.9 μm transition, as will be shown later.

Although some values are reported in literature for the ETU parameter of Nd-doped vanadates [4, 5], the temperature dependence of such parameters has not been investigated so far: in previous work we demonstrated a strong temperature-dependence of the ETU macroparameter in Nd:YAG [6] and here we use the same z-scan technique to probe the analogous dependence in Nd:YVO$_4$ and Nd:GdVO$_4$.

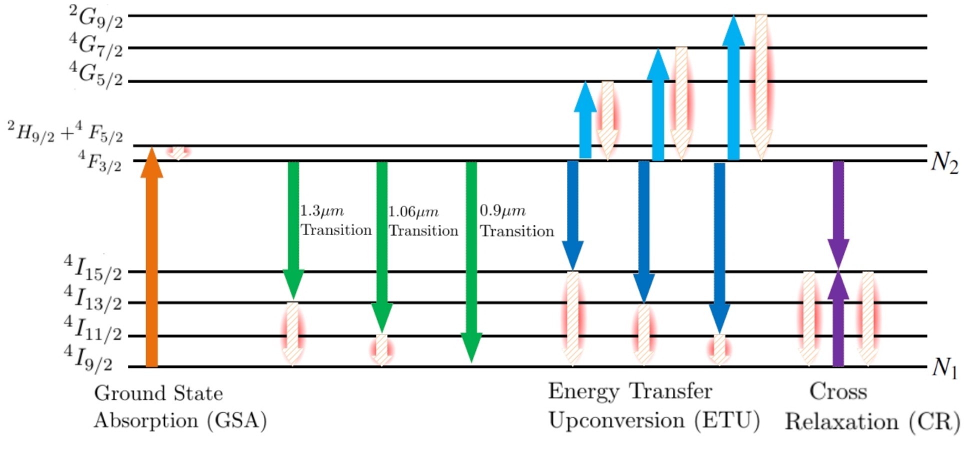

Fig. 1. Schematics of the Nd^{3+} Energy levels and ETU dynamics.

In addition in this work, we present a comprehensive study of the absorption cross section into the $^2H_{9/2} + ^4 F_{5/2}$ energy levels, over the range of temperatures from RT to $450K$. These results, which show a decrease in peak cross section with increasing temperature, were key to the characterisation of the macroscopic ETU parameter over the same range of temperatures.

In the z-scan technique the incident pump irradiance is controlled by scanning a sample through the focus of a laser beam, and the change in transmission is then related back to the input irradiance (position). We compared the measured transmission curve to the prediction of a spatially dependent two-level rate-equation model, using the ETU coefficient as the only fitting parameter.

Via this z-scan method we determined the ETU parameter. The attempt to probe the strong absorption π-polarisation 808 nm peak resulted in a too weak transmission. Therefore, in order to obtain more suitable transmission signals, the pump laser was tuned to both the strongest 808 nm, and weaker 806 nm, peaks of the σ-polarisation, which gave compatible results. ETU was found to decrease from $(3.2 \pm 0.7)\ 10^{-16}\ cm^3/s$ to $(1.8 \pm 0.4)\ 10^{-16}\ cm^3/s$ and $(5.0 \pm 0.5)\ 10^{-16}\ cm^3/s$ to $(3.4 \pm 0.2)\ 10^{-16}\ cm^3/s$ for 0.6at.% and 1at.% Nd:YVO_4 respectively, and $(3.3 \pm 0.5)\ 10^{-16}\ cm^3/s$ to $(0.8 \pm 0.2)\ 10^{-16}\ cm^3/s$ and $(5.5 \pm 0.5)\ 10^{-16}\ cm^3/s$ to $(3.1 \pm 0.3)\ 10^{-16}\ cm^3/s$ for 0.5at.% and 1.1at.% Nd:$GdVO_4$.

This information, coupled with elevated temperature emission cross section data [7], provide a new level of detail for the design parameters needed for these materials, which may have direct impact on further optimisation of vanadate lasers operating at elevated temperatures or under intense pumping conditions.

2. Methodology

2.1. Absorption cross section

Small signal absorption measurements, well described by the Beer-Lambert law, can provide an accurate measure of the absorption cross section or the doping ion concentration, once the other parameters are known.

Beer-Lambert law describes how light is absorbed as it propagates inside a material:

$$I_{out}(\lambda) = I_{in}(\lambda)\ e^{-\alpha_{abs}(\lambda)L} = I_{in}(\lambda)\ e^{-\sigma_{abs}(\lambda)C_{\%}N_0L} \tag{1}$$

where I_{out} is the transmitted irradiance, I_{in} is the pump-laser incident irradiance, $\alpha_{abs}(\lambda)$ is the absorption coefficient per unit length, $\sigma_{abs}(\lambda)$ is the absorption cross section, L is the length of the crystal, $C_{\%}$ the doping-ion percentage, with N_0 the density of doping-ions at 1at.%.
Inverting eqn. (1) we have

$$\frac{\alpha_{abs}(\lambda)}{N_0} = \sigma_{abs}(\lambda)C_{\%} = \frac{\ln(\frac{I_{in}(\lambda)}{I_{out}(\lambda)})}{N_0L} \tag{2}$$

We recorded the input and the transmission spectra of the broadband amplified spontaneous emission (ASE) of a LIMO fibre-coupled diode-laser. Enabling the calculation of I_{in}/I_{out}, once the corrections due to Fresnel reflections at the uncoated facets of the crystal for the appropriate polarisation state, were made.

To determine $C_{\%}$, the usual practice is to measure $\alpha_{abs}(\lambda)$ for a fixed wavelength λ^*, usually one corresponding to the strongest absorption line, and applying Eqn. (2), with $\sigma_{abs}(\lambda^*)$ known from trusted sources. In order to minimise the error on the doping ion concentration determination, or rather, increase the confidence in its value, we employed eqn. (3).

$$C_{\%} = \frac{\alpha_{abs}(\lambda^*)}{\sigma_{abs}(\lambda^*)N_0} = \frac{\ln(\frac{I_{in}(\lambda^*)}{I_{out}(\lambda^*)})}{\sigma_{abs}(\lambda^*)N_0L} \tag{3}$$

Using several different values of λ_i, corresponding to different absorption peaks of known $\sigma_{abs}(\lambda_i)$, and averaged, the (ideally identical, but in reality not) results:

$$C_{\%} = \frac{1}{N}\sum_{i=1}^{N} c_{\%,i} = \frac{1}{N}\sum_{i=1}^{N} \frac{\alpha_{abs}(\lambda_i)}{\sigma_{abs}(\lambda_i)N_0} \tag{4.1}$$

$$\Delta C_{\%} = \sqrt{\frac{1}{N-1}\sum_{i=1}^{N} |c_{\%,i} - C_{\%}|^2} \tag{4.2}$$

where N is the total number of absorption lines used and Eqn. (4.2) is the standard deviation from the average, the uncertainty associated to our concentration measurement.

Once we established the doping ion concentration for our 4 samples, we thoroughly characterised the ${}^2H_{9/2} +^4 F_{5/2}$ absorption cross section and its dependence upon temperature by applying eqn. (2) and retrieving the absorption cross section spectra $\sigma_{abs}(\lambda)$ in the range RT to $450K$.

2.2. ETU model and data interpretation

The z-scan technique has been previously used to determine the magnitude of the ETU parameter for various rare-earth ions in different host media [6, 8–10]. It consists in scanning the sample through the waist of a converging/diverging pump beam, thus enabling the scaling of the input irradiance from values significantly lower than (small-signal transmission regime) to ones comparable to, or higher than, the saturation irradiance. The transmission through the sample with respect to each z-scan position (irradiance) is compared to the predictions of the spatially dependent two-level rate-equation model (5), described in detail in [6].

$$\frac{\partial N_1(r,z)}{\partial t} = -\frac{I_p(r,z)}{h\nu_p}\sigma_{abs}N_1(r,z) + \frac{N_2(r,z)}{\tau_f} + W_{ETU}N_2(r,z)^2 \tag{5.1}$$

$$\frac{\partial N_2(r,z)}{\partial t} = \frac{I_p(r,z)}{h\nu_p}\sigma_{abs}N_1(r,z) - \frac{N_2(r,z)}{\tau_f} - W_{ETU}N_2(r,z)^2 \tag{5.2}$$

$$\frac{dI_p(r,z)}{dz} = I_p(r,z)(-\sigma_{abs}N_1(r,z)) \tag{5.3}$$

where for the neodymium-doped host $N_1(r,z)$ is the population density of the ground state ${}^4I_{9/2}$, $N_2(r,z)$ is the population density of the excited state ${}^4F_{3/2}$, σ_{abs} is the measured absorption cross section at the pump photon energy $h\nu_p$, and W_{ETU} is the macroscopic ETU coefficient to be determined. The parameter τ_f is the measured fluorescence lifetime in the small signal transmission regime (i.e. weak excitation densities) and it accounts for both the intrinsic lifetime of the sample in question and the cross relaxation rate [11]. I_p is the spatial pump irradiance distribution that changes according to (5.3), which was characterised through a preliminary automated beam quality measurement and confirmed to be Gaussian within the experimental errors.

The pump transmission through the sample at each step of the z-scan, corresponding to different beam sizes, was calculated by numerically solving the system of Eqs. (5) for a fixed power P_{in}, measured beam dimensions, and by iteratively calculating the variation of $I_p(r,z)$, accounting for the Gaussian spatial distribution and its dependence upon $N_1(r,z)$. In order to facilitate the computation and increase the density of the grid used for the iterative calculation (300 radial and 1000 longitudinal steps), system (5) was solved for the steady state conditions $\partial N_i/\partial t = 0$ $(i = 1, 2)$. Using these conditions and (6.1), N_1 was obtained from the analytical solution of (5.1), (6.2).

$$N_2(r,z) = N_{tot} - N_1(r,z) = C_{\%}N_0 - N_1(r,z) \tag{6.1}$$

$$N_1(r,z) = \frac{-b \pm \sqrt{b^2 - 4ac}}{2a} \tag{6.2}$$

$$a = W_{ETU}$$

$$b = \frac{I_p(r,z)}{h\nu_p}\sigma_{abs} - \frac{1}{\tau_f} - 2W_{ETU}N_{tot}$$

$$c = \frac{N_{tot}}{\tau_f} + W_{ETU}N_{tot}^2$$

At the end of the iteration steps the transmitted irradiance $I_t(r,z)$ is integrated over the effective beam area in order to obtain the transmitted pump power P_t, to compare the simulated transmittance, $T_{th} = P_t/P_{in}$, with the measured one. The automated data collection focussed on the minimisation of the uncertainty associated with the fixed parameters of model (5). The automated setup shown in Fig. 2 was employed to first perform M^2 measurements of the Ti:sapphire pump-laser, and, successively, z-scan measurements.

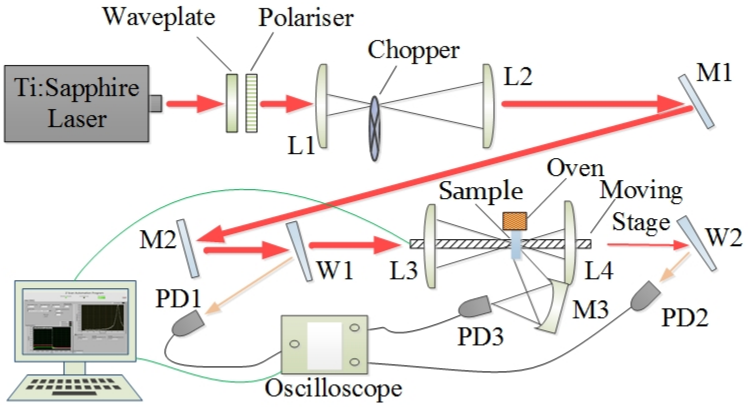

Fig. 2. Automated ETU measurement setup. Lenses: L_1 (f = 50 mm), L_2 (f = 300 mm), L_3 (f = 200 mm), L_4 (f = 175 mm); high reflectivity mirrors at 808 nm: M_1 and M_2 flat, M_3 curved (radius or curvature=100 mm); glass wedges: W_1 and W_2; Si photodiodes: PD_1, PD_2 and PD_3.

The pump's beam quality parameter M^2 was measured with a wedge positioned after the focussing lens, and a CCD beam profiling camera (Spiricon), obtaining $M^2_{x,y} = (1.06 \pm 0.01)$, $w_x = (19.7 \pm 0.2)$ μm and $w_y = (19.9 \pm 0.2)$ μm. The z-scan setup was calibrated in order to retrieve quantitative relations between the voltages produced by the reference and transmission photodiodes PD_1 and PD_2 and the power after the 200 mm moving lens (L_3), i.e. incident power P_{in}, and before the 175 mm moving collection lens (L_4), i.e. transmitted power P_t, respectively. Once determined, the analytical forms of the relations were obtained by fitting polynomial curves to the calibration data, $P_{in} = f(V_{PD_1})$ and $P_t = g(V_{PD_2})$, which could always precisely quantify P_{in} and P_t from PD_1 and PD_2's voltage readings. The goodness of the calibration was verified by making sure that z-scan measurements performed with no sample in the setup always returned, after the conversion of voltages into powers, a transmittance of (100 ± 1)%.

The way the errors associated to each modelling parameter affected the resultant ETU parameter was evaluated by propagating the uncertainties associated to these parameters through the numerical model (5). It was established that the power instability of the pump beam dominated.

Therefore, constant and precise monitoring of the incident and transmitted powers (voltages) through a LabView driven interface mitigated the Ti:sapphire power instabilities by fixing a suitable tolerance window for the input power: the measurements corresponding to incident powers outside the allowed band were discarded. Furthermore, the transmittance measurement was repeated multiple times, of the order of 50 samples, at each z-scan position, in order to increase the confidence in the measured value and at the same time determine an uncertainty on each data point given by the standard deviation from the mean as defined in (4.2).

Defining a band, whose limits were $\bar{T}_z \pm \Delta T_z$, the data was fitted to the model (5), giving outlying curves corresponding to limiting ETU values that established the error on the final result.

The fitting procedure is based on the minimisation of the sum of the squared residuals defined as

$$S^2(W_{ETU}) = \sum_z \left[(T_z - T_{th}(z, W_{ETU}))^2\right] \tag{7}$$

where the dependence of the theoretical transmission value $T_{th}(z)$ (calculated numerically from model (5)) on the ETU parameter W_{ETU} is emphasised, because the latter is the minimising parameter being sought.

The same fitting procedure was employed for the measurement of the small-signal fluorescence lifetime: theoretical model (8)

$$V(t) = V_0\, e^{-\frac{t}{\tau_f}} \tag{8}$$

was fitted to the fluorescence waveform collected at each step of the z-scan (sample in Fig. 3) by using V_0 and τ_f as fitting parameters. We only accounted for the data collected in the small signal transmission regime, obtaining a number of usable waveforms in the order of 100 and a typical dispersion around the average result of $\sim 1\%$, that gave us good confidence in the resulting value for the fluorescnce lifetime, moderated by the cross relaxation process. The fluorescence signal was monitored throughout the z-scan: the effect of ETU in shortening the lifetime in the high irradiance regime can be observed in Fig. 3. Unlike [12], this shortened lifetime could not be used to determine the ETU macroparameter due to the Gaussian distribution of the pump beam.

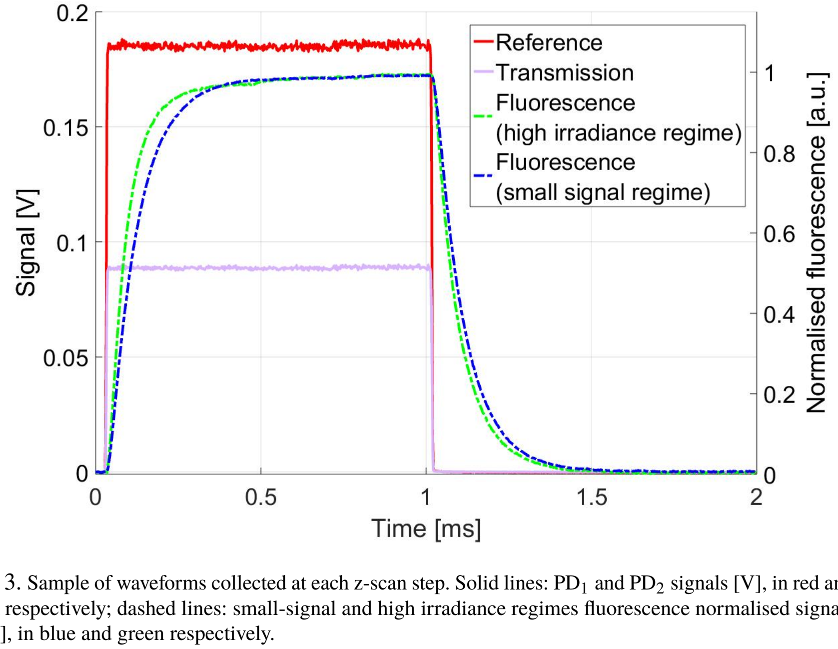

Fig. 3. Sample of waveforms collected at each z-scan step. Solid lines: PD_1 and PD_2 signals [V], in red and pink respectively; dashed lines: small-signal and high irradiance regimes fluorescence normalised signals [a.u.], in blue and green respectively.

3. Absorption cross section measurements

3.1. Experimental setup

The setup employed for the small signal absorption measurements, shown in Fig. 4, comprising a simple symmetric telescope, coupling the broadband amplified spontaneous emission (ASE) of a sub-threshold fibre-coupled diode-laser (LIMO60-F200-DL808) to the sample under test. The incident 6 mW ASE, extending for $\sim$ 40 nm around 808 nm, was collimated by lens L_1 ($f = 30$ mm) and focused by lens L_2 ($f = 150$ mm) onto the analysed sample. The incident light was polarised with a polariser. The transmitted light was re-collimated by lens L_3 ($f = 150$ mm) and finally re-imaged into a fibre-coupled Optical Spectrum Analyser (ANDO AQ6317B) by lens L_4 ($f = 30$ mm). When probing different polarisations, the setup was kept fixed, and the crystal rotated, providing access to both π- and σ- polarisations for the anisotropic vanadate crystals.

A beam radius of 500 μm with a confocal parameter of $b \simeq 36$ mm was produced in the sample.

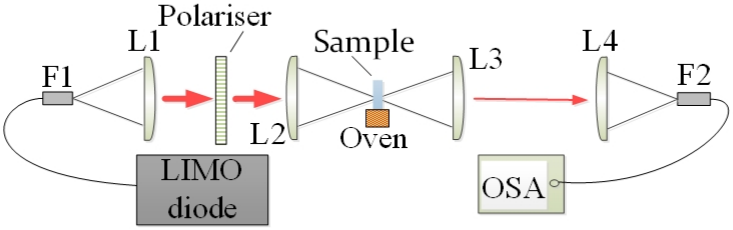

Fig. 4. Absorption measurements setup.

The input, $P_{in}(\lambda)$, and the transmitted, $P_{out}(\lambda)$, power spectra of the diode were recorded with a resolution of 0.05 nm using the OSA. Given our experimental conditions that the beam size doesn't vary significantly over the crystal length ($L \ll b$, with $L \simeq 1mm$), the equivalence

$$\frac{I_{in}(\lambda)}{I_{out}(\lambda)} = \frac{P_{in}(\lambda)}{P_{out}(\lambda)} \tag{9}$$

could be made.

The crystal was positioned on a heated copper mount, whose temperature could be changed in the range from RT to $450K$. We could thus characterise the absorption cross section of Nd:YVO_4 and Nd:$GdVO_4$ for several different elevated temperatures by applying eqn. (2).

3.2. Results and discussion

With small signal absorption measurements performed in the band 780 – 830 nm around the peak absorption at 808 nm, for both polarisations σ-pol and π-pol, there were on the order of 7 peaks available (N). We obtained the results summarised in table 1 for the doping-ion concentrations of the respective samples and associated errors, assuming reference peaks from [13].

Table 1 **Doping Ion Concentration Measurements: Results And Associated Uncertainties.**

Sample analysed	Nominal $C_{\%}$ [%]	Measured $C_{\%}$ [%]	Measured $\Delta C_{\%}$ [%]
Nd:YVO_4	0.5	0.60	0.02
Nd:YVO_4	1.0	0.97	0.02
Nd:$GdVO_4$	0.5	0.54	0.03
Nd:$GdVO_4$	1.0	1.15	0.03

We characterised the absorption cross section at elevated temperatures: measuring the absorption coefficient for the two different concentrations of the available crystals in the range from RT to 450K and, using the parameters $C_{\%}$ in table 1, we retrieved the absorption cross section spectra. From the excellent agreement between the spectra of the different concentrations of the same kind of samples (Nd:YVO_4 and Nd:$GdVO_4$) we confirmed the goodness of the previous doping-ion concentration measurements. The results are shown in Fig. 5 and 6.

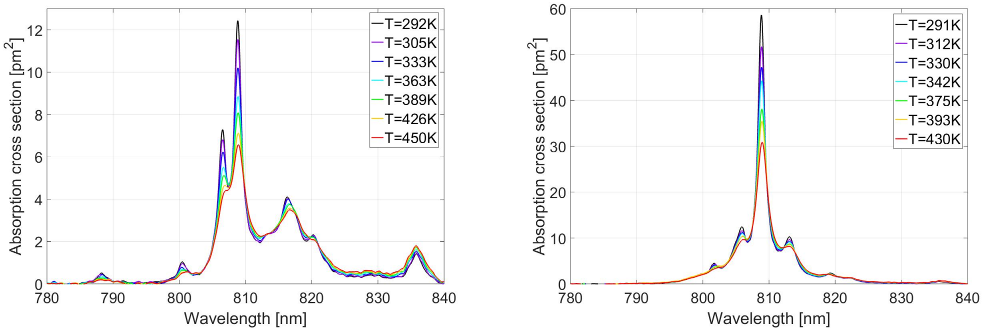

(a) σ-pol.

(b) π-pol.

Fig. 5. Nd:YVO_4 absorption cross section.

The highest peak for the π-polarisation absorption cross section of Nd:YVO_4, centred at (808.90 ± 0.05) nm, decreased from (58.6 ± 0.2) pm^2 at 291K to (30.9 ± 0.6) pm^2 at 430K, the bandwidth (FWHM) broadened from (1.25 ± 0.02) nm to (2.29 ± 0.02) nm, and red-shifted (0.20 ± 0.05) nm at the highest temperature. The maximum value for the σ-polarised spectrum, centred at (808.80 ± 0.05) nm, reduced from (12.4 ± 0.2) pm^2 to (6.6 ± 0.2) pm^2, also red-shifting by (0.20 ± 0.05) nm over the whole temperature range.

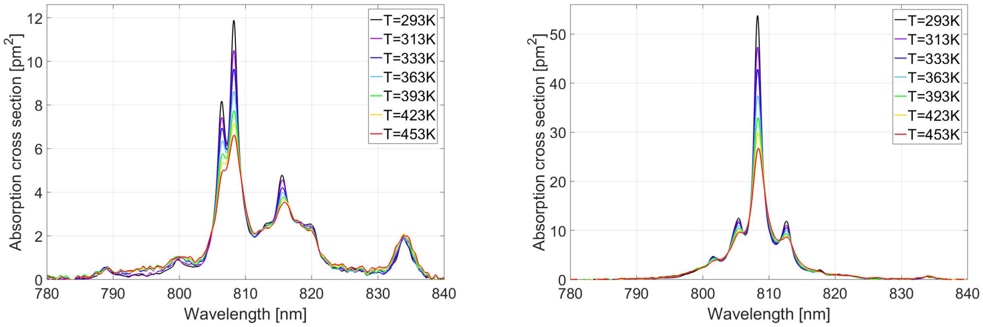

(a) σ-pol.

(b) π-pol.

Fig. 6. Nd:$GdVO_4$ absorption cross section.

Similarly, for Nd:$GdVO_4$ the strongest peak is for the π-polarisation absorption cross section, centred at (808.60 ± 0.05) nm, decreasing from (54.0 ± 0.3) pm^2 at 293K to (25.7 ± 0.5) pm^2 at 453K and broadening from (1.51 ± 0.02) nm to (2.74 ± 0.02) nm. The σ-polarisation strongest peak, centred at (808.80 ± 0.05) nm, decreases from (11.9 ± 0.2) pm^2 at 293K to (6.6 ± 0.1) pm^2 at 453K. Both peaks show a (0.10 ± 0.05) nm redshift from the RT, at the highest temperature.

We retrieved the maximum amplitude of the strongest peaks for both polarisations and fitted the data sets of absorption cross section vs temperature to polynominal functions. In all cases, a second degree polynomial of the kind (10) proved satisfying in describing the experimental data (Fig. 7(b)).

$$\sigma_{abs}(T) = p_1 + p_2 T + p_3 T^2 \tag{10}$$

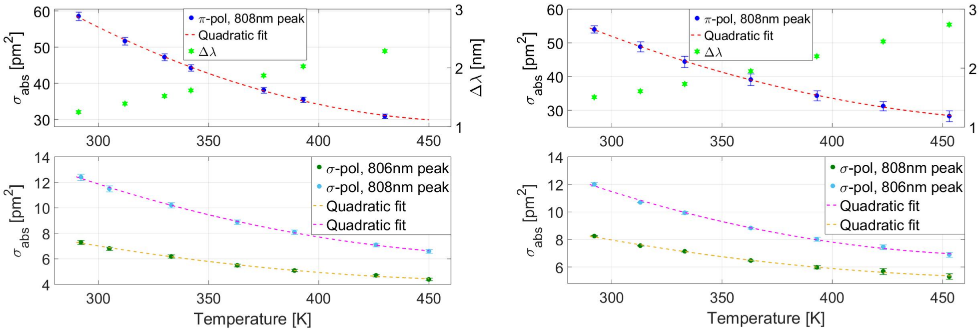

(a) Nd:YVO$_4$. (b) Nd:GdVO$_4$.

Fig. 7. Polynomial fits to the dependence of absorption cross section peaks vs temperature. Secondary y-axis: FWHM ($\Delta\lambda$) for the π-pol peaks vs temperature.

The obtained fitting coefficients are summarised in tables 2(a) and 2(b).

Table 2 Second Degree Polynomial Fit Coefficients For σ_{abs} Vs T Dependence.

Peak λ [nm]	p_1	p_2	p_3
808 (π)	221.56	-0.809	8.5e-4
808 (σ)	40.28	-0.135	1.3e-4
806 (σ)	21.91	-0.071	7.2e-5

2(a) Nd:YVO$_4$.

Peak λ [nm]	p_1	p_2	p_3
808 (π)	176.04	-0.586	5.7e-4
808 (σ)	38.82	-0.132	1.4e-4
806 (σ)	22.53	-0.069	7.0e-5

2(b) Nd:GdVO$_4$.

4. ETU coefficient measurements

4.1. Experimental setup

As shown in Fig. 2, the output beam of the continuous-wave Ti:sapphire laser passes through a $\lambda/2$ waveplate that defines the polarisation direction. A polariser, with its transmission axis aligned to the table top, is placed right after the waveplate. The combined action of these two components allowed the tuning of the incident power. This configuration also let us probe the different axes of the examined samples by simply turning the sample by 90^o according to the axis we required access to.

Lenses L_1 (f=50 mm) and L_2 (f=300 mm) provide a 6x telescope that expands the beam to a size suitable to obtain second moment beam radii $w_x = (19.7 \pm 0.2)$ μm and ($w_y = 19.9 \pm 0.2$) μm after the moving lens L_3 (f=200 mm). A mechanical chopper modulates the Ti:sapphire beam with a pulse width ~ 1 ms, a long enough time for the crystal's population to reach steady state, while short enough to avoid significant localised heating of the sample.

A fraction of the collimated beam is directed to the photodiode PD$_1$ by an uncoated glass wedge W$_1$: this provides the reference signal to the oscilloscope. The second wedge W$_2$, after L$_4$, reflects some of the transmitted signal to the photodiode PD$_2$, providing the transmitted signal to the oscilloscope. The curved mirror M$_3$ (radius of curvature=100 mm) images the resulting fluorescence from the pumped region on to the fast photodiode PD_3.

The sample is placed on the same controlled heating stage used for measuring the absorption cross sections. The automation is coordinated through LabView and consists in a common linear translation stage (Stackshot) for the lenses L_3 and L_4. At each (adjustable-length) step of the scan the communication between the oscilloscope (Agilent model MSO6104A) and the LabView interface allows the collection of the captured waveforms (sample in Fig. 3), repeated for as many times as required.

4.2. Results and discussion

Figures 8(a) and 8(b) show the results for the investigated Nd:YVO_4 and Nd:$GdVO_4$ samples. The ETU parameter's magnitude decreases with temperature and concentration, showing two distinct curves for the different concentrations tested: it decreases from $(3.2 \pm 0.7)\ 10^{-16}\ cm^3/s$ to $(1.8 \pm 0.4)\ 10^{-16}\ cm^3/s$, and $(5.0 \pm 0.5)\ 10^{-16}\ cm^3/s$ to $(3.4 \pm 0.2)\ 10^{-16}\ cm^3/s$ for 0.6at.% and 1at.% Nd:YVO_4 respectively, and $(3.3 \pm 0.5)\ 10^{-16}\ cm^3/s$ to $(0.8 \pm 0.2)\ 10^{-16}\ cm^3/s$ and $(5.5 \pm 0.5)\ 10^{-16}\ cm^3/s$ to $(3.1 \pm 0.3)\ 10^{-16}\ cm^3/s$ for 0.5at.% and 1.1at.% Nd:$GdVO_4$. The two crystal types show similar values and overall trends.

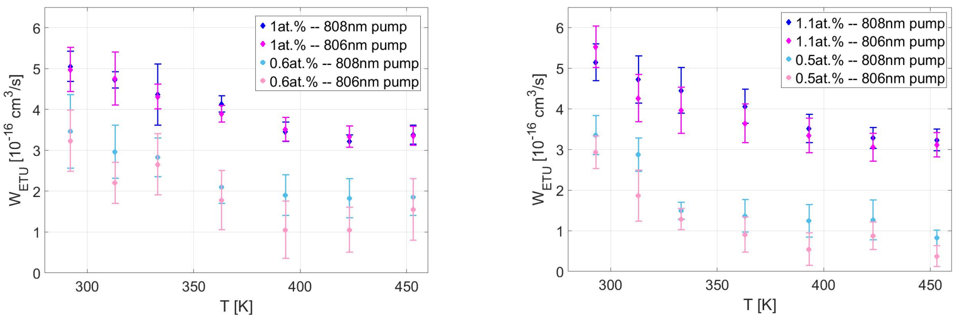

(a) Nd:YVO_4.

(b) Nd:$GdVO_4$.

Fig. 8. Results for the ETU parameter measurements.

We use an analytical formula, given in [14], to calculate the incident threshold pump power P_{th} of a laser cavity, including ETU (11). This model is applied to a simple linear cavity, comprising: a plane input mirror coated on one facet of a 1 mm long Nd:YVO_4 crystal, and a 90%R, 50 mm radius of curvature, output-coupler mirror positioned to provide a 49 mm long resonator, as described in detail in [15]. Accounting for the temperature dependence of the absorption cross section, emission cross section [7] and ETU parameter, as well as fractional populations within each Stark manifold given by the temperature-dependent Boltzmann distribution, we quantify the temperature-dependent effects of ETU. Note any additional temperature rise in the gain medium due to the pumping cycle has been neglected in this analysis. The laser-threshold is compared for the cases of operation on the 0.9 μm quasi-four-level and 1.06 μm true four-level transitions of 0.5at.% and 1.0at.% doped Nd:YVO_4. Similar results are expected for the corresponding

Nd:GdVO$_4$ crystals.

$$\begin{aligned} P_{th} \simeq & \frac{h\nu_p \pi w_p^2}{2(f_1+f_2)\sigma\tau_f\eta_q\eta_{LP}\eta_a}\left(L_T + 2f_1\sigma\eta_{LP}N_{tot}l_r\right) \\ & \left[1 + W_{ETU}\frac{\tau_f\alpha_{abs}}{4(f_1+f_2)\sigma\eta_{LP}}\left(L_T+2f_1\sigma\eta_{LP}N_{tot}l_r\right)\right] = \\ & = P_{th}(withoutETU)\left[1+W_{ETU}\frac{\tau\alpha_{abs}}{4(f_1+f_2)\sigma\eta_{LP}}\left(L_T+2f_1\sigma_{em}\eta_{LP}N_{tot}l_r\right)\right] \end{aligned} \tag{11}$$

where $h\nu_p$ is the pump energy, w_p is the pump spot size, f_1 and f_2 are the fractional populations of ground and excited laser levels respectively, σ is the Stark-to-Stark-level cross section, τ_f is the fluorescence lifetime of the excited state, η_q is the pump quantum efficiency, η_{LP} is the spatial operlap factor between pump and laser mode spot sizes, η_a is the pump absorption efficiency, L_T is the cavity loss factor, N_{tot} is the unpumped population, l_r is the crystal length, W_{ETU} is the ETU macroparameter, α_{abs} is the absorption coefficient at the pump wavelength.

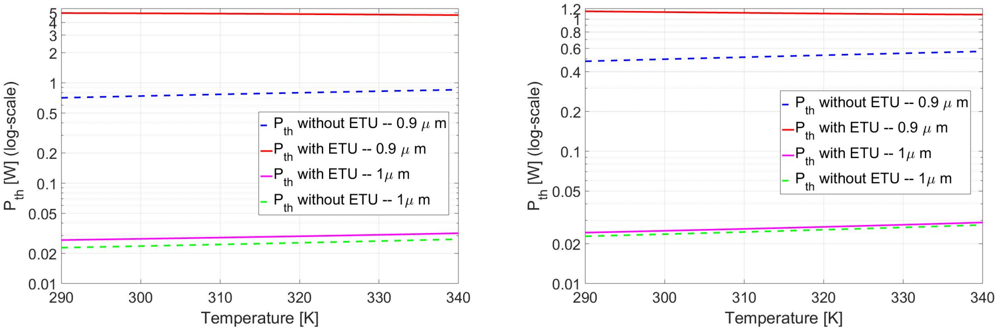

(a) Nd:YVO$_4$, 1.0at.%.

(b) Nd:YVO$_4$, 0.5at.%.

Fig. 9. P_{th} vs Temperature for a 1mm thick Nd:YVO$_4$ sample.

The results in Fig. 9(a) show that, besides the known fact that the threshold for the quasi-four-level system is higher than the one for the four-level system, the 1 μm transition is barely affected by the ETU process ($P_{th} \simeq 23mW$ without ETU versus $P_{th} \simeq 27mW$ with). Instead, the 0.9 μm transition is critically affected by it, resulting in a more than 5x increase for the 1at.% crystal, that only slightly decreases with increasing temperature.

The results for the 0.5at.% crystal are significantly better: while the 1 μm transition is equally not significantly affected by ETU, the difference in the 0.9 μm transition threshold is slightly more than 2 times larger when including ETU effects.

Although a preliminary analysis, this description clearly shows the challenge for the quasi-four-level Nd-vanadate system, when accounting for ETU. Furthermore, the pump power density to achieve threshold for the 0.9 μm transition would introduce a strong temperature rise and thermo-optical aberrations, increasing the cavity losses even further with negative feedback implications. Additionally, for quasi-four-level operation with the vanadate hosts, the extreme gain at 1 μm will provide a further challenge through gain depletion caused by the strong ASE.

4.3. *Conclusions*

In conclusion, we have presented a general way of determining with high confidence the doping-ion concentration in a sample of known absorption cross section spectrum, and have undertaken a detailed study of the temperature dependence of the polarised absorption cross section for Nd:YVO$_4$ and Nd:GdVO$_4$. Furthermore, we have performed automated z-scan measurements for 0.5at.% and 1.0at.% nominal doping-levels of the respective samples, finding that the ETU coefficient decreases with increasing temperature and decreasing doping level. This data and the available emission cross section data has allowed us to estimate the laser threshold pump power for a simple cavity, highlighting the challenges for quasi-four-level laser operation, dramatically enhanced by the effects of ETU. As is generally empirically known these results reaffirm the advantage in the use of low-dopant concentration samples in order to minimise deleterious thermal effects and optimise laser performance. Moreover, operation at elevated temperatures will have little impact for Nd:vanadate lasers operating at 1 μm.

Funding

Engineering and Physical Sciences Research Council (EPSRC) (EP/J008052/1).

Acknowledgments

S. Cante and J. I. Mackenzie acknowledge support from EPSRC. Data presented can be found at DOI: https://doi.org/10.5258/SOTON/D0328.